Reorganizing Pt surface water structure for highly efficient alkaline hydrogen oxidation reaction

Chengzhang Wan[1,2], Zisheng Zhang[1], Sibo Wang[1], Qiang Sun[3], Ershuai Liu[3], Heting Pu[1,2], Ao Zhang[2], Zhengyue Chen[1], Aamir Hassan Shah[1], Xiaoyang Fu[1], Anastassia N. Alexandrova[1,2,4], Qingying Jia[3], Yu Huang*[2,4], Xiangfeng Duan*[1,4]

[1]Department of Chemistry and Biochemistry, University of California, Los Angeles; California 90095, United States; [2]Department of Materials Science and Engineering, University of California, Los Angeles; California 90095, United States; [3]Department of Chemistry and Chemical Biology, Northeastern University, Boston, Massachusett, 02115, United States; [4]California NanoSystems Institute, University of California, Los Angeles; California 90095, United States.

The hydrogen oxidation reaction (HOR) in alkaline electrolytes exhibits markedly slower kinetics than that in acidic electrolytes. This poses a critical challenge for alkaline exchange membrane fuel cells (AEMFCs). The slower kinetics in alkaline electrolytes is often attributed to the more sluggish Volmer step (hydrogen desorption). It has been shown that the alkaline HOR activity on the Pt surface can be considerably enhanced by the presence of oxophilic transition metals (TMs) and surface-adsorbed hydroxyl groups on TMs (TM-OH_{ad}), although the exact role of TM-OH_{ad} remains a topic of active debates. Herein, using single-atom Rh-tailored Pt nanowires as a model system, we demonstrate that hydroxyl groups adsorbed on the Rh sites (Rh-OH_{ad}) can profoundly reorganize the Pt surface water structure to deliver record-setting alkaline HOR performance. *In-situ* surface characterizations, together with theoretical studies, reveal that surface Rh-OH_{ad} could promote oxygen-down $H_2O_\downarrow$ configuration that favors more hydrogen bond with Pt surface adsorbed hydrogen ($H_2O_\downarrow \cdots H_{ad}$-Pt) than that of hydrogen-down configuration ($OH_{2\downarrow}$). The $H_2O_\downarrow$ further serves as the bridge to facilitate the formation of an energetically favorable six-membered-ring transition state with neighboring Pt-H_{ad} and Rh-OH_{ad}, thus reducing the Volmer step activation energy and boosting HOR kinetics.

Hydrogen fuel cells offer an appealing alternative to internal combustion engines for reducing greenhouse gas emissions in the transportation industry.[1] The current commercial proton exchange membrane fuel cells (PEMFCs) generally require a substantial amount of costly Pt-based catalysts to facilitate the sluggish oxygen reduction reaction (ORR) in acidic electrolytes, which constitutes a critical roadblock preventing the widespread adoption of PEMFCs.[2] On the other hand, the ORR reaction in alkaline exchange membrane fuel cells (AEMFCs) can be facilitated by cost-effective nonprecious-metal-based catalysts.[3-6] However, the hydrogen oxidation reaction (HOR) at the anodes exhibits markedly slower kinetics in alkaline media, which is often attributed to a more sluggish Volmer step (hydrogen desorption).[7-13] Even with the most favorable Pt catalysts, the HOR in alkaline media is at least two orders of magnitude slower than that in acidic media.[14] Thus, in AEMFCs, the bottleneck shifts from the cathodic ORR step to the anodic HOR.

It has been shown that the alkaline HOR activity on the Pt surface can be considerably enhanced by the presence of oxophilic transition metals (TMs) and surface-adsorbed hydroxyl groups on TMs ($TM\text{-}OH_{ad}$),[14-23] although the exact role of $TM\text{-}OH_{ad}$ remains a topic of active debates. Some studies suggested that the $TM\text{-}OH_{ad}$ could directly interact with $Pt\text{-}H_{ad}$ to reduce apparent hydrogen binding energy and promote the hydrogen desorption step,[20,24-26] while others suggested that the major role of surface $Pt\text{-}OH_{ad}$ is improving the hydrogen transfer across the electrical double-layer rather than modulating the energy barrier of the hydrogen desorption.[13]

Recent theoretical studies suggested that the interfacial water orientation plays a critical role in modulating the pH-dependent HOR kinetics on pure Pt surface.[11,21,27-30] There are three general types of interfacial water configurations, hydrogen-down water ($OH_{2\downarrow}$), oxygen-down ($H_2O_{\downarrow}$), and parallel water ($H_2O^{=}$). The $H_2O_{\downarrow}$ can increase the hydrogen desorption rate via the hydrogen bond between the O end of the water molecule and the $Pt\text{-}H_{ad}$ ($Pt\text{-}H_{ad}\cdots{}_{\downarrow}OH_2$), while the $OH_{2\downarrow}$ reduces the hydrogen desorption rate via the repulsion between the H end of the water molecule and $Pt\text{-}H_{ad}$.[11,27] Under the alkaline HOR condition, the Pt surface has much less $H_2O_{\downarrow}$ (6.3%) than that under the acidic condition (13.9%) due to the positive shift of the point of zero free charge (PZFC) with increasing pH, resulting in lower HOR activity.[27] In this regard, a plausible physical picture is that $TM\text{-}OH_{ad}$ could modulate the interfacial water orientation, and in turn, modulate the HOR kinetics indirectly. However, experimental proof of the surface water structure reorganization has been elusive.

Herein, using single-atom Rh-tailored Pt nanowires (SARh-PtNWs) as a model system (Fig. 1a), we systematically investigate the interfacial water structure to unravel the role of Rh-OH_{ad} in reorganizing the Pt surface water structure for enhanced HOR kinetics. Electrochemical studies demonstrate that SARh-PtNWs deliver a significantly enhanced alkaline HOR specific activity (SA) of 10 mA/cm^2, 17 times higher than the PtNWs. *In-situ* X-ray absorption spectroscopy (XAS) analysis reveals the existence of the surface adsorbed hydroxyl (OH_{ad}) on the single-atom Rh sites (Rh-OH_{ad}) and the oxygen down $H_2O_{\downarrow}$ near the Pt/Rh interface within the HOR potential region. Molecular dynamics (MD) simulations further reveal that the Rh-OH_{ad} moieties can modulate the surface water structure to promote the $H_2O_{\downarrow}$ configuration around the Pt atoms adjacent to the Rh-OH_{ad}. Such reoriented $H_2O_{\downarrow}$, other than the Rh-OH_{ad}, serves as the critical H_{ad} acceptor, which further bridges the Pt-H_{ad} and Rh-OH_{ad} to form an energetically favorable six-membered-ring transition state (Fig. 1b) with a markedly reduced Volmer step activation barrier.

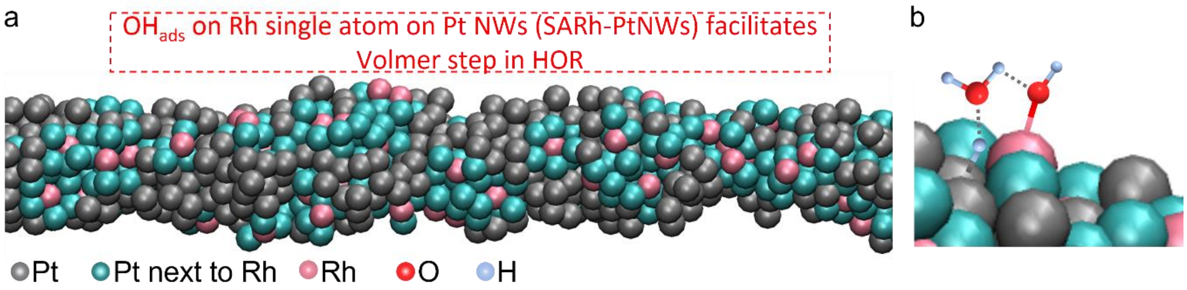

Fig. 1|Schematic illustration of single-atom Rh tailored Pt nanowires (SARh-PtNWs) and the Rh-OH mediated six-membered-ring transition state of Volmer step.

Results and discussion

Structure characterizations

The SARh-PtNWs were synthesized using a one-pot solvothermal synthesis process (Methods). The transmission electron microscopy (TEM) studies show an ultrafine one-dimensional (1D) morphology (Fig. 2a). The high-angle annular dark-field scanning TEM (HAADF-STEM) studies reveal a crystalline structure with a lattice space of 0.22 nm (Fig. 2b) and an average diameter of 1.3 nm (Fig. 2c). Energy-dispersive X-ray spectroscopy (EDS) analysis reveals a uniform distribution of Rh along the PtNWs with an Rh/Pt ratio of 1:20 (Fig. 2d).

The Fourier-transform extended X-ray absorption fine structure (EXAFS) spectroscopy of the SARh-PtNWs dry electrode shows no noticeable Rh-Rh peak at 2.39 Å (all radial distances reported here without phase correction), but two peaks located at 1.53 Å and 2.69 Å (Fig. 2e). This result suggests Fitting of the EXAFS spectra suggest that these two peaks can be assigned to Rh-O scattering with an Rh-O coordination number (CN) of 3.8±0.5 and Rh-Pt scattering with an Rh-Pt CN of 3.0±1.0 (Supplementary Fig. 1 and Table 1). The high Rh-Pt CN suggests that the majority of the Rh atoms are heavily oxidized exposed to air and thus reside on the surface. The high Rh-Pt CN plus absence of Rh-Rh scattering, which is also seen *in-situ* shown in the next section, further suggests that they are atomically dispersed in the single-atom form in the Pt matrix of SARh-PtNWs. On the other hand, the Pt L_3-edge EXAFS spectrum of the SARh-PtNWs closely resembles that of Pt foil, absence of the Pt-O scattering peak at 1.5 Å (Fig. 2f), which indicates the Pt in the SARh-PtNWs is predominately in the metallic phase.

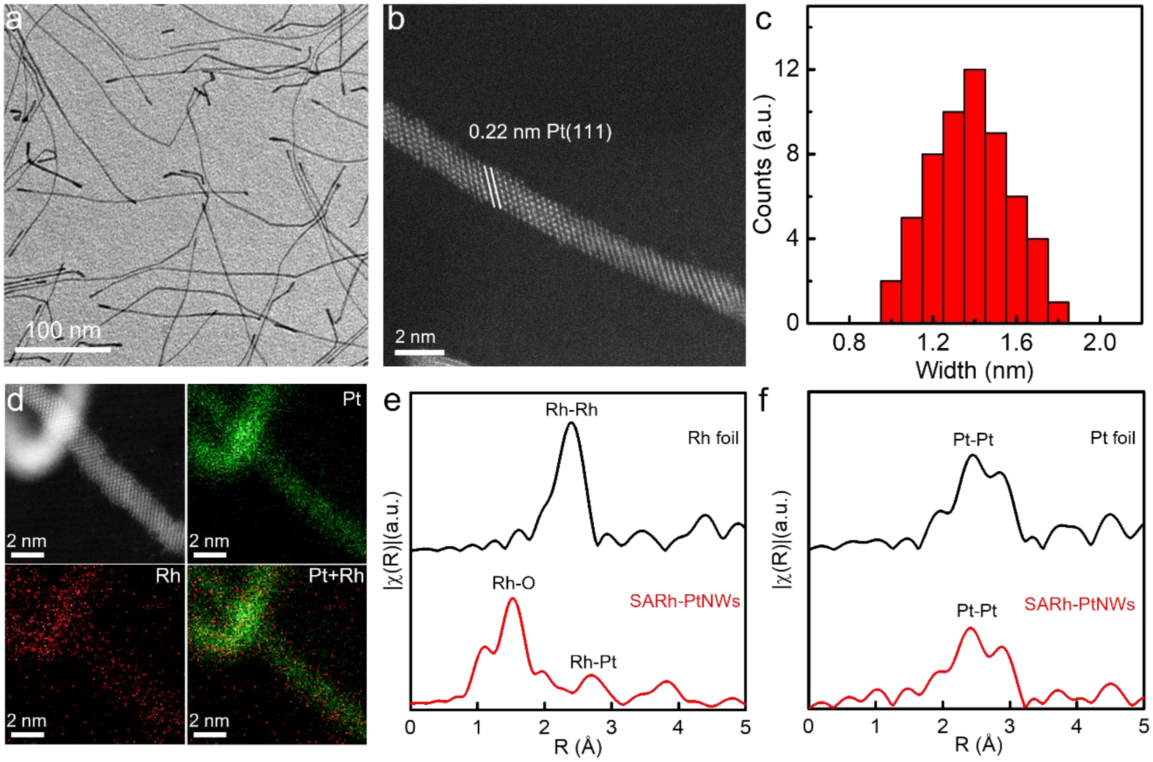

Fig. 2|Structural characterizations. (**a**) Representative TEM images of SARh-PtNWs. (**b**) HAADF-STEM image of SARh-PtNWs. (**c**) Diameter distribution of SARh-PtNWs. (**d**) EDS-mapping of SARh-PtNWs. (**e**) The Rh K-edge EXAFS spectra of SARh-PtNWs and Rh reference foil. (**f**) The Pt L_3-edge EXAFS spectra of SARh-PtNWs and the Pt reference foil.

Electrochemical characterization

We next evaluated the alkaline HOR activity of the SARh-PtNWs against two reference samples, PtNWs and RhNWs (Fig. 3a and b). In comparison, the SARh-PtNWs show a significantly enhanced HOR specific activity (SA, normalized by electrochemically active surface area) of 10 mA/cm^2 at 0.05 V vs. reversible hydrogen electrode (V_{RHE}), which is 17-fold and 30-fold higher than that of pristine PtNWs and RhNWs, respectively (Fig. 3b). The corresponding mass activity (MA, normalized by overall metal loading) of SARh-PtNWs at 0.05 V_{RHE} (7.5 A/mg) is also significantly higher than that of the PtNWs (0.38 A/mg) and RhNWs (0.33 A/mg). Both the SA and MA of SARh-PtNWs also represented the best values achieved among all Pt-based HOR catalysts reported to date (Supplementary Fig. 2).[16,31-40]

To further understand the role of the SARh decorations on the HOR kinetics, we examined cyclic voltammetry (CV) of these samples in 1 M KOH (Fig. 3c-e and Supplementary Fig. 3), which showed highly distinct features in the hydrogen desorption region (Fig. 3c-e). The pure PtNWs exhibit a typical H_{ad} desorption profile: with a broad Pt(111) peak below 0.4 V_{RHE} and two sharp peaks at 0.26 V_{RHE} and 0.36 V_{RHE}, corresponding to H_{ad} desorption on the Pt (110) facet and the Pt(100) facet, respectively (Fig. 3c). The SARh-PtNWs show even broader hydrogen desorption peaks for all three facets with attenuated Pt(110) and Pt(100) peaks (Fig. 3d), suggesting a stronger repulsive lateral interaction among the H_{ad}.[41] Additionally, **a new hydrogen desorption peak is observed in SARh-PtNWs at 0.16** V_{RHE}**, which is tentatively ascribed to the H desorption at the Pt/Rh interface** (Fig. 3d).

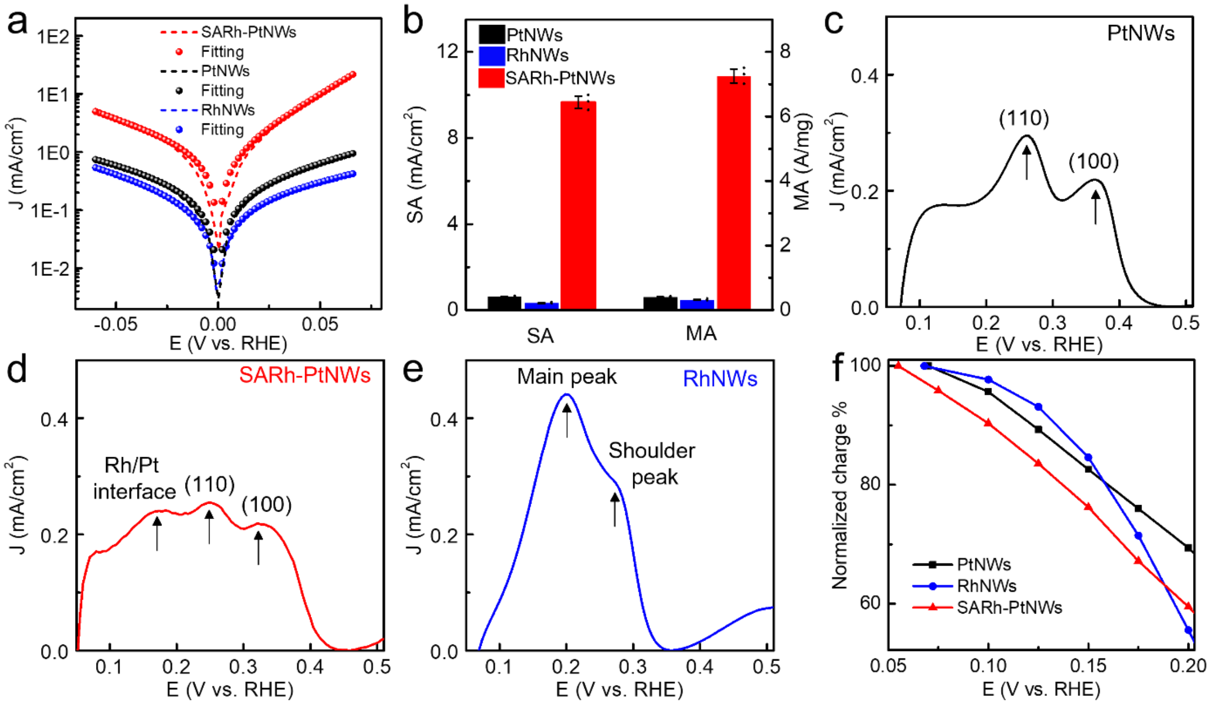

Fig. 3| Electrochemical characterizations. (**a**) HER/HOR polarization curve for PtNWs, SARh-PtNWs, and RhNWs (normalized by electrochemically active surface area). (**b**) Comparison of HOR SA and MA for

PtNWs, SARh-PtNWs and RhNWs. The error bars represent the standard deviation (SD) with n=3. The hydrogen desorption characteristics of (**c**) PtNWs, (**d**) SARh-PtNWs and (**e**)RhNWs. The current density is normalized by electrode geometry surface area. The double layer capacitance has been subtracted from the CV in Supplementary Fig. 3. (**f**) The accumulative H desorption characteristics in the anodic scan.

Compared with the PtNWs and the SARh-PtNWs, the pure RhNWs show a distinct sharp peak of hydrogen desorption at 0.20 V_{RHE} and a shoulder peak at 0.27 V_{RHE} (Fig. 3e), lower than the peaks of 0.26 V_{RHE} and 0.37 V_{RHE} for Pt NWs. This lower peak potential is usually considered as the indication of weaker H binding and faster HOR kinetics. However, the RhNWs showed the lowest H desorption current density in the potential range below 0.1 V_{RHE} among all three samples (Fig. 3c-e), suggesting that the hydrogen desorption on RhNWs at lower potential is not favorable, consistent with the literature that Rh has higher HBE than Pt.[42]

The integration of the hydrogen desorption peak further reveals that the SARh-PtNWs show the fastest hydrogen desorption rate below 0.10 V_{RHE} (Fig. 3f), followed by the PtNWs and the RhNWs. Importantly, **since H_{ad} at low surface hydrogen coverage are mostly at fcc sites while the real intermediates are H_{ad} on atop sites that exist under high coverage,[43,44] the H desorption rate at high hydrogen coverage potential regime (close to 0 V_{RHE}) is more closely correlated with the overall HOR activity**.[43] Since the HOR in the alkaline condition is limited by the hydrogen desorption step, the faster hydrogen desorption rate near 0 V_{RHE} could offer an important signature indicating relative activity expected among three catalysts (SARh-PtNWs > PtNWs > RhNWs), consistent with the measured activity trend (Fig. 3a and b).

In-situ XAS characterization of SARh-PtNWs.

The alkaline HOR kinetics follows the Tafel-Volmer mechanism in which the sluggish Volmer step is the rate-determining step (rds). It is hypothesized that the modified Pt surface with higher oxophilicity can effectively reduce the Volmer step barrier, which has been tentatively attributed to the surface-absorbed OH_{ad} in the HOR potential range, although it is difficult to experimentally prove the existence of such early-adsorbed OH_{ad}. Thus, we have conducted *in-situ* XAS to probe the evolution of the local coordination environment and oxidation states of Rh and Pt within the HOR potential region and their role in the HOR kinetics.

Compared with the *ex-situ* EXAFS of the SARh-PtNWs showing a notable Rh-O peak (black line in Fig. 4a), the *in-situ* studies at 0 V_{RHE} (red line in Fig. 4a) reveal that the Rh-O peak decreases markedly along with a notable increase of the Rh-Pt peak. EAXFS fitting gives an average Rh-O

CN of 0.6 at 0 V_{RHE}, suggesting that only at most one oxygen atom remains at 0 V_{RHE}. Meanwhile, the Rh-Pt CN increases from 3.0 to 7.8 (Supplementary Fig. 4 and Table 1). Such a high Rh-Pt CN suggests that most of the single Rh atoms are anchored **inside** the surface Pt layer, forming Rh-Pt alloying bonding. Moreover, the Rh-O peak shifts from 1.56 Å *ex-situ* to 1.62 Å at 0 V_{RHE} (Fig. 4a, Supplementary Fig. 4) suggesting an elongated Rh-O bond that is quantitatively confirmed by EXAFS fitting (Supplementary Table 1). This result suggests a weaker Rh-O interaction at 0 V_{RHE}. Together, these *in-situ* studies demonstrate the partial removal of O and the reconstruction of Rh local coordination structure under reducing potential. Meanwhile, the *in-situ* EXAFS studies at 0 V_{RHE} at the Pt edge reveal that there is no Pt-O coordination (Supplementary Table 2); and the XANES spectrum nearly overlapping that of a Pt foil indicates the Pt oxidation state of SARh-PtNWs is essentially the same as that of Pt foil (Supplementary Fig. 5). This result suggests a metallic Pt surface without appreciable Pt-O interactions (Pt-OH_{ad}), and confirming that the majority of oxygen species are adsorbed on the Rh sites at 0 V_{RHE}.

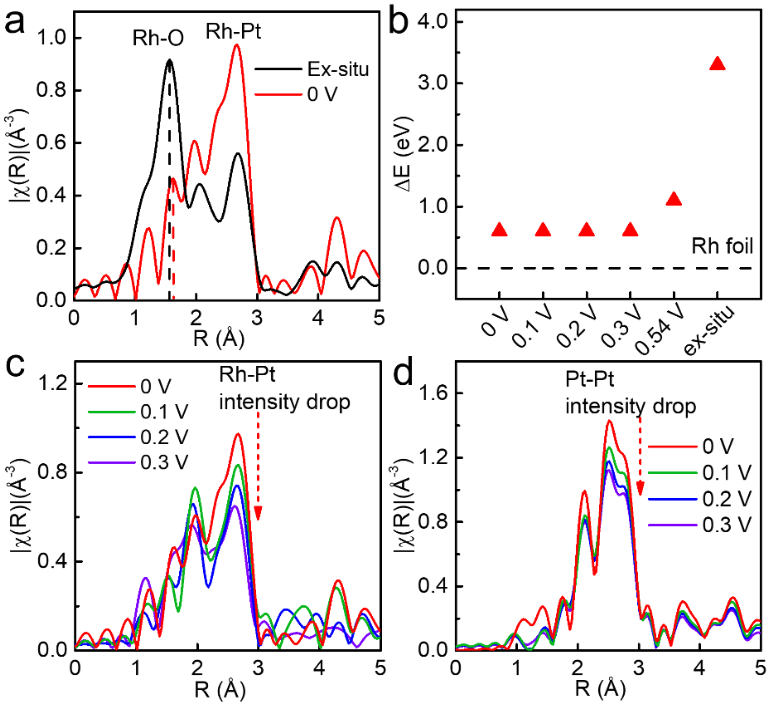

Fig. 4| *In-situ* XAS characterization of SARh-PtNWs. (**a**) The Rh K-edge EXAFS spectra under 0 V_{RHE} and 0.54 V_{RHE}; the positive shift of Rh-O peak at 0 V_{RHE} (red dashed line) as compared with 0.54 V_{RHE} (black dashed line) indicates a slightly elongated Rh-O bonding and therefore a weaker Rh-O interaction. (**b**) The difference (ΔE) in the energy of the edge position of the Rh K-edge XANES spectra of SARh-PtNWs collected from 0 to 0.54 V_{RHE} and *ex-situ*, and that of a Rh reference foil (Supplementary Figure 6). The edge position is commonly defined as the X-ray energy where the normalized absorption of an XANES spectrum is precisely one-half. The Rh single atom at 0 V_{RHE} is slightly oxidized and the oxidation state does not change until 0.3 V_{RHE}. The EXAFS spectra of Rh (**c**) and Pt (**d**) from 0 to 0.3 V_{RHE}. The intensity drop of the Rh-Pt peak and the Pt-Pt peak indicates the increased population of $H_2O_{\downarrow}$ (at higher potential) that blocks the metal-metal interaction.

Within the potential region relevant to the HOR kinetics of Pt and Rh (0-0.3 V_{RHE}) in alkaline media, the possible oxygen species are either OH_{ad} or $H_2O_{\downarrow}$, or a mixture of both. We have further collected the *in-situ* XANES spectra within this potential region to identify the adsorbed oxygen species. The edge energy of Rh at 0 V_{RHE} is 0.6 eV more positive than that of the Rh foil reference, indicating that Rh atoms are slightly oxidized at 0 V_{RHE} (Fig. 4b, Supplementary Fig. 6). Since the $H_2O_{\downarrow}$ is charge-neutral and should not lead to significant oxidation state change, the oxygen species that accounts for the higher Rh oxidation state is thus ascribed to the weakly adsorbed OH_{ad}.

Considering the HOR potential region is more than 0.6 V below the PZFC of Pt in the alkaline media (around 1.0 V_{RHE}), the Pt surface is negatively charged in this potential regime,[18] which repels the O end of water molecules to form a predominantly H-down $OH_{2\downarrow}$ configuration. It is recognized that $OH_{2\downarrow}$ configuration has a negligible effect on the Pt-Pt scattering peak intensity while the $H_2O_{\downarrow}$ could block the Rh-Pt and Pt-Pt scattering and significantly suppress their peak intensities.[21,45] The *in-situ* EXAFS spectra of Pt/C show little decrease of Pt-Pt EXAFS peak from 0.04 to 0.24 V_{RHE} (Supplementary Fig. 7), consistent with the expectation that the $OH_{2\downarrow}$ configuration dominates the pure Pt surface under this potential regime.

In contrast, *in-situ* EXAFS spectra of SARh-PtNWs reveal a notable attenuation of Rh-Pt and Pt-Pt peak intensity from 0 V_{RHE} to 0.3 V_{RHE} (Fig. 4b-d) while without apparent oxidation of either Rh or Pt since the corresponding XANES spectra nearly overlap (Figure 4b; Supplementary Fig. 5-6). These results suggest the increased surface population of $H_2O_{\downarrow}$ that blocks the Rh-Pt and Pt-Pt signals. We hypothesize that such distinct behavior between the pure Pt surface and the Rh-tailored Pt surface can be attributed to the surface Rh-OH_{ad} that reorganizes the surface water structure and stabilizes the $H_2O_{\downarrow}$ via hydrogen bonding, which is verified by density functional theory (DFT) calculations as shown next.

Theoretical study

We further applied DFT calculations to resolve the role of the Rh-OH_{ad} in the enhanced HOR kinetics from the energetics point of view. Our calculation shows that the adsorption energy of OH is -2.82 eV on Pt(111) and -3.11 eV on the Rh site on Pt(111), indicating a preferential adsorption of OH_{ad} on Rh sites. With OH_{ad}, Rh shows a more positive Bader charge (+0.47 |e|) than Pt (+0.27 |e|) (Supplementary Fig. 8), suggesting stronger binding with negatively charged O in OH_{ad}.

To study the distribution of interfacial water structure at the solid/liquid interface under HOR potential range, we further carry out fixed-potential *ab initio* molecular dynamics (FPMD) simulations with a hybrid implicit/explicit hybrid solvation scheme (Supplementary Fig. 9) at 0 V_{RHE} and pH=14. The representative snapshot of water structure on Pt(111) surface shows that interfacial water on the Pt surface is dominated by $OH_{2\downarrow}$ configuration (Fig. 5a). In contrast, $H_2O_\downarrow$ can favorably adsorb on the Pt site adjacent to the Rh site in Rh-OH/Pt(111) (Fig. 5b), which is stabilized by the hydrogen bond with the OH_{ad} on the adjacent Rh and stays adsorbed throughout the FPMD simulation. The spatial distribution of interfacial water at equilibrium, from statistics of the height of water molecules relative to the surface (Fig. 5c), shows two major peaks for O (in H_2O): the first peak at about 2.3 Å corresponds to the water with O bound to the surface Pt atoms ($H_2O_\downarrow$), and the second peak at about 3.1 Å corresponds to the first layer of free unbound water ($OH_{2\downarrow}$). In comparison, **the first peak for the Rh-OH/Pt(111) surface exhibits a substantially larger intensity than that for pure Pt(111) (Fig. 5c), indicating a much higher $H_2O_\downarrow$ population in the presence of Rh-OH species**. The increased population of $H_2O_\downarrow$ on Rh-OH_{ad}/Pt surface persists at higher coverages of H_{ad} (0.5 ML) (Supplementary Fig. 10).

Atomic insights into the role of the Rh-OH_{ad} and the $H_2O_\downarrow$ in HOR kinetics are further investigated by calculating the free energy profile of the Volmer step (H_{ad} transfer to OH_{ad} or interfacial H_2O) at a relevant H_{ad} coverage of 0.5 monolayer, using constrained FPMD sampling and thermodynamic integration. The initial state (IS) of Pt(111) shows a surface water structure that is dominated by $OH_{2\downarrow}$ configuration (Fig. 5d), which needs to reorient to a flat configuration in the transition state (TS) to interact with the H_{ad} (Fig. 5d), showing a larger barrier of 0.65 eV (Fig. 5f).

In contrast, the IS of Rh-OH/Pt(111) shows a water structure with an $H_2O_\downarrow$ molecule on the Pt atom adjacent to the Rh-OH_{ad} (Fig. 5e). The $H_2O_\downarrow$ bridges between Pt-H_{ad} and Rh-OH_{ad}, serving as an H relay and forming an energetically favorable six-member ring TS (Fig. 5e) that substantially reduces the Volmer step barrier to 0.48 eV (Fig. 5f). The energetic and geometric evidence clearly confirms that the **surface Rh-OH_{ad} could help reorganize near-surface water**

structure and stabilize $H_2O_{\downarrow}$ configuration, which in turn facilitates the formation of an energetically favorable six-membered-ring transition state with Pt-H_{ad}, thus reducing the Volmer step activation energy and boosting HOR kinetics.

It should be noted that the proposed reaction pathways here are distinct from the previously suggested bifunctional mechanism, in which the Pt-H_{ad} is generally perceived to directly react with the OH_{ad} on the metal surface or OH^- in the electrolyte to form H_2O.[14,46] Our calculation reveals that the direct reaction between Pt-H_{ad} and adjacent Rh-OH_{ad} exhibits a higher Volmer step barrier (0.53 eV) due to its highly-strained four-member-ring transition state (Supplementary Fig. 11) and is thus kinetically less favorable.

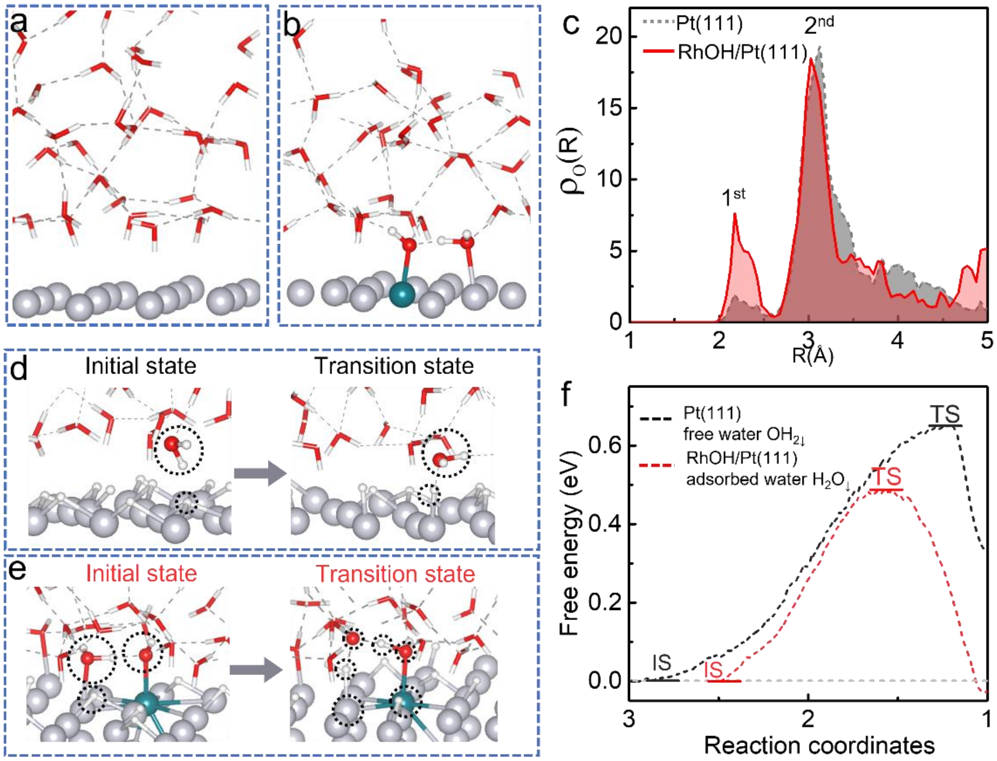

Fig. 5| Water distribution and free energetics from fixed-potential molecular dynamics simulations. (**a**) The snapshot of water structure on the pure Pt(111) surface. (**b**) The snapshot of water structure on the Rh-OH/Pt(111) surface at zero H_{ad} coverage, where the oxygen-down $H_2O_{\downarrow}$ is stabilized on the Pt site adjacent to Rh-OH_{ad}. (**c**) The distribution function of oxygen (from water) as a function of distance from the top surface of pure Pt(111) and Rh-OH/Pt(111) at zero H_{ad} coverage. (**d**) The representative snapshots of the IS and TS of the primary Volmer step pathway on Pt(111) surface using free $OH_{2\downarrow}$as the H_{ad} acceptor at 0.5 monolayer H_{ad} coverage. (**e**) The representative snapshots of the IS and TS of the primary Volmer step reaction pathway on RhOH/Pt(111) surface using $H_2O_{\downarrow}$ as the bridge to form a six-member-ring transition state (marked by black dotted circle in TS) at 0.5 monolayer H_{ad} coverage. (**f**) Free energy barriers from thermodynamic integration for Volmer step reaction pathways on Pt(111) with $OH_{2\downarrow}$as the H_{ad} acceptor and RhOH/Pt(111) with $H_2O_{\downarrow}$ as the H_{ad} acceptor at 0.5 monolayer H_{ad} coverage.

Conclusion

By using SARh-PtNWs as a model system, we determined the role of Rh-OH_{ad} in boosting the alkaline HOR of Pt via reorganizing the Pt surface water structure. The single-atom Rh decoration presents as surface Rh-OH_{ad} in the HOR potential range, which promotes the $H_2O_{\downarrow}$ configuration on Pt atoms adjacent to Rh-OH_{ad} and forms an energetically favorable six-membered-ring transition state, resulting in a remarkably lower Volmer step activation barrier. The electrochemical studies demonstrate greatly enhanced HOR kinetics in the SARh-PtNWs, delivering the highest specific activity and mass activity of 10 mA/cm^2_{Pt} and 7.5 A/mg_{Pt} at 0.05 V_{RHE} in 1 M KOH. The demonstrated role of interfacial water structure in determining the alkaline HOR kinetics provides critical insights into establishing a detailed molecular-level understanding of HOR kinetics at the Pt/water interface for the rational design of next-generation fuel cell technologies.

Methods

Chemicals

Platinum(II) acetylacetonate [$Pt(acac)_2$, Pt 48.0%], hexachloroplatinic acid [H_2PtCl_6], Rh(III) acetylacetonate [$Rh(acac)_3$, 95%], Glucose, Tungsten(0) hexacarbonyl ($W(CO)_6$, 97%), (+)-Sodium l-ascorbate (98%), Oleylamine (>98%), 1-Octadecene (ODE, >90%), Polyvinylpyrrolidone (M.W. 40000), N,N-dimethylmethanamide (DMF) and Nafion® 117 solution (~ 5%) were purchased from Sigma Aldrich. Commercial Pt/C catalyst (10 wt% Pt, and particle size ~ 2 nm) was purchased from Alfa Aesar. Carbon supported platinum nanoparticles (Pt/C, 47.2 wt%) purchased from Tanaka Kikinzoku Kogyo were used for XAS. Ethanol (200 proof) was obtained from Decon Labs, Inc. Potassium hydroxide (KOH) was purchased from Fisher Chemical. All the above reagents were used as received without further purification. Carbon black (Vulcan XC-72) was received from Cabot Corporation and was annealed for 2 hours under Ar gas environment at 400 °C before being used. The deionized water (18 MΩ/cm) was obtained from an ultra-pure purification system (Milli-Q advantage A10). The Naftion^{TM} 117 (PEM) and the Fumasep Fas-50 (AEM) were purchased from the Fuel cell Store.

Synthesis of SARh-PtNWs

In a 30 mL glass vial, 20 mg $Pt(acac)_2$, 5mg $Rh(acac)_3$, 1.6 mg $W(CO)_6$, 135 mg glucose, and 60 mg PVP were dissolved in a mixture of 3 mL oleylamine and 2 mL octadecene. The mixture was sonicated for 1 hour and purged Ar for 5 min. The resulting homogenous solution was kept at 140

°C for 8 hours. After the reaction, the precipitate was centrifuged at 12100 r.p.m. and washed with ethanol/hexane (25 mL/5 mL) for three times. The final product was suspended in 10 mL cyclohexane. In a 30 mL glass vial, 15 mg carbon black (the carbon black was annealed under Ar at 200 °C for 1 hour before use) was sonicated in 15 mL ethanol for 1 hour. 10 mL SARh-PtNWs hexane solution was then added into the carbon black/ethanol solution and the mixture was sonicated for another 1 hour. The catalysts were centrifuged at 12100 r.p.m. and washed with cyclohexane/ethanol solution three times, followed by being dried in the vacuum oven for 1 hour.

Synthesis of PtNWs

100 mg H_2PtCl_6 solution (8 wt %) and 500 mg KOH were added to a mixed solution containing 4 mL of ethylene glycol (EG) and 6 mL of N,N-dimethylmethanamide (DMF). After sonicating for 1 h, the resultant homogeneous solution was transferred into a 25 mL Teflon-lined autoclave and heated at 170 °C for 8 h. The black products were collected and washed with ethanol and DI water three times and dispersed in the ethanol.

Synthesis of RhNWs

10 mg of Na_3RhCl_6, 40 mg sodium ascorbate, 160 mg PVP, and 85 mg KI were dissolved in 1 mL DI water after ultra-sonication. Then 5 mL EG was added and mixed as a homogenous mixture. Then the vial was heated at 170 °C for 2 h. After cooling to room temperature, the products were collected via centrifugation after the addition of acetone. The products were then washed via ultra-sonication/centrifugation in the solvent combination of ethanol/acetone for 1 time and ethanol/hexane for 2 times. The final products were dispersed in ethanol for further study after ultra-sonication.

Characterizations

Transmission electron microscopy (TEM) images were taken on an FEI T12 operated at 120 kV. Atomic resolution high angle annular dark-field scanning transmission electron microscopy (HAADF-STEM) images and X-ray energy dispersive spectroscopy (EDS) mapping were taken on FEI Titan Cubed Themis G2 300 at 200 kV and JEOL Grand ARM 300CF TEM/STEM with double spherical aberration-correctors operated at 300 kV. Samples for TEM measurements were prepared by dropping 10-20 μL nanoparticles dispersion in hexane on a carbon-coated copper grid (Ladd Research, Williston, VT). The composition of catalysts was determined by inductively coupled plasma atomic emission spectroscopy (ICP- AES, Shimadzu ICPE-9000) as well as SEM-EDS (JEOL JSM-6700F FE-SEM).

X-ray absorption spectroscopy collection and analysis

The ink for the XAS electrodes was composed of ethanol, 5 wt% Nafion solution (Aldrich), and catalyst powders. The ink was sprayed onto carbon paper on a glass slide heated under 40 °C. The Rh loading is around 0.25 mg/cm^2. The XAS experiments were conducted at room temperature in a previously described *in situ* spectro−electrochemical half−cell[47] in which continuously H_2 purged 1.0 M KOH aqueous solution was circulated. Before being transferred into the cell, the electrodes were conditioned in 0.1 M $HClO_4$ under vacuum for 40 minutes to remove surface oxides and contaminants. Full-range Pt L_3-edge and Rh K-edge spectra were taken at various static potentials along the anodic sweep of the cyclic voltammetry (CV). Data were collected on the same electrode in transmission mode at the Pt L_3-edge and fluorescence mode at the Rh K-edge, with a Pt/Rh reference foil positioned between I2 and I3 as a reference. The voltage cycling limits were 0.05 to 0.5 V_{RHE}. Data collection was performed at the chosen potentials held during anodic sweeps. The electrode was fully cycled following each potential hold in order to clean the electrode surfaces after each potential hold. The data at the beamlines 7-BM (QAS) and 8-ID (ISS) in National Synchrotron Light Source II (NSLS-II) (Brookhaven National Laboratory, NY). Typical experimental procedures were utilized with details provided in our previous work.[48] The data were processed and fitted using the Ifeffit−based Athena[49] and Artemis[50] programs. Scans were calibrated, aligned and normalized with background removed using the IFEFFIT suite.[51] The $\chi(R)$ were modeled using single scattering paths calculated by FEFF6.[52]

Electrochemical Measurements

To obtain a homogeneous catalyst ink, 1 mg of dried catalysts was mixed with 1 mL ethanol and sonicated for 5 minutes. Then, 10 µL (20 µL for stability test) of Nafion (5 wt%) was added to the solution. After sonication, 20 µL of the homogeneous ink was dropped onto a 5 mm diameter glassy carbon electrode (0.196 cm^2, Pine Research Instrumentation). The ink was dried under ambient air before electrochemical testing.

All electrochemical tests were carried out in a three-electrode cell from Pine Research Instrumentation. The working electrode was a glassy carbon rotating disk electrode (RDE) coated with corresponding catalysts. The reference electrode was an Hg/HgO electrode from CH

Instrument and was calibrated in 1.0 M KOH with saturated H_2. A graphite rod was used as the counter electrode. Cyclic voltammetry was conducted in 1.0 M KOH between 0.05 to 1.1 V_{RHE} at a sweep rate of 100 mV/s. The polarization curves were tested between --0.2-0.5 V_{RHE} at a sweep rate of 5 mV/s in 1.0 M. The solution resistances were measured via an impedance test. ECSA was measured through the hydrogen desorption region in N_2-saturated 1.0 M KOH.

Computational Methods:

Model Set-up

In the static calculations, all surfaces are modeled based on an orthogonalized 4-layer 4x4 supercell of Pt(111) termination. The bottom two layers of the Pt slab are constrained as bulk regions, and everything else is allowed to relax as the interface region. A vacuum slab of 15 Å thickness is added in Z direction to avoid spurious interactions between periodic images.

In the molecular dynamics simulations, 36 explicit water molecules (water slab is c.a. 10 Å thick) are placed above the surface for more realistic description of the interfacial solvation structures. The water configurations are pre-equilibrated using the TIP4P force field.[53]

Surface Rh sites are introduced by substituting a Rh atom for a surface Pt atom. H_2O_{ad} and OH_{ad} are tested to be the most stable on atop sites. The 0.5 ML H_{ad} configurations are pre-equilibrated using FPMD simulation, starting from a uniformly distributed configuration.

Electronic structure methods

The periodic electronic structure calculations are performed with density functional theory, using PBE functional[54] and PAW pseudopotentials[55] implemented in the VASP program (version 5.4.1).[56-59] D3 correction is used to account for the dispersion interactions.[60] Gaussian smearing with 0.1 eV width is used. The convergence criterion for SCF electronic minimization is set to 10^{-5} eV. Due to the relatively large system and sampling size, only the Γ *k*-point is sampled in the reciprocal space of the Brillouin zone throughout, and the cutoff energy for the kinetic energy of the plane-waves is 400 eV.

The solvation effect and electrolyte distribution beyond the slab regions are described implicitly by a polarizable continuum with linearized Poisson-Boltzmann model as implemented in the VASPsol code.[61] The dielectric constant is taken as 78.4 (water), and the Debye length is taken as 3 Å.

All periodic electronic structure analyses are performed based on converged charge density or wavefunction. The Bader charges are calculated using Bader Charge Analysis program.[62]

Fixed-potential Treatment

Under a constant electrode potential, the electrode surface is effectively a grand canonical ensemble of electrons where the system can exchange electrons with the electrode (electron reservoir) until the work function of the system aligns with the electrode potential. This treatment has been demonstrated to be necessary in investigating the potential-dependent geometric changes and energetics at an electrochemical interface.[63,64]

Here we use the fixed-potential method as implemented in the EChO Python package (https://github.com/zishengz/echo). To be specific, the number of electrons is being optimized in an outer iteration after SCF convergence of each ionic step (geometry optimization step or MD step) to adjust the work function of the system to align with the given electrode potential. This treatment does not depend on the constant capacity approximation or interpolation and hence can exactly capture the potential dependent geometric changes and the resulting shift in potential of zero charge and effective capacity.

Due to the difficulty in continuously adjusting the number of hydroxide ions in the explicit solvation model within the pH range of interest, the pH effect at a constant potential in RHE scale is modeled by shifting the potential in SHE according to the Nernst equation:

$$U_{\mathrm{RHE}} = U_{\mathrm{SHE}} + \ln 10\ k_{\mathrm{B}}T\ \mathrm{pH}$$

Fixed-potential ab initio Molecular Dynamics Simulations

The ab initio molecular dynamics simulations are performed on the pre-equilibrated structures and with the same DFT settings as in the geometry optimization. The nuclear motions are treated under the Born-Oppenheimer approximation, with a time step of 0.5 fs. The simulation is performed within the NVT ensemble at 300 K using the Langevin thermostat (with a friction coefficient of 0.1) which has been demonstrated to cause the least inconsistency of local temperature in solid/liquid interfacial models.[65] To study the interfacial dynamics at different pH, we perform a series of simulations at different potentials in the SHE scale (corresponding to the pH values via the Nernst equation), without explicitly introducing hydronium or hydroxide ions which is not compatible with the hybrid solvation scheme. The potential is controlled at a constant value during the simulation by adjusting the number of electrons in the system according to a linear potentiostating step (factor of 0.5 e/V) after each nuclear motion. Each simulation is run for about 10 ps in total, and only the last 5 ps of the trajectory (the more equilibrated portion, as shown in Supplementary Figure 9) are used for statistical analysis.

Fixed-potential Free Energy Calculations

The free energy profiles are obtained by constrained FPMD sampling and thermodynamic integration. Here we adopt the slow-growth approach[66] where the reaction coordinate ξ (defined as the distance between the transferred H_{ad} and the acceptor O atom) is constrained and varied by 0.005 Å per fs during the FPMD simulation. The duration of each sampling is about 5 to 10 ps (varies for different collective variables). The change in ξ is sufficiently slow, so that the system can be viewed as ever-equilibrated during the sampling. The resulted trajectory constitutes a blue-moon ensemble, and the free energy gradient can be calculated by tracking the generalized force along the constraint. Integrating the free energy gradient with respect to ξ yields the free energy profile.

It should be noted that, due to the artifact of the explicit/implicit solvation scheme, charged species would exhibit unphysical electronic structure and dynamics. Specifically, the counter-charge density generated by the implicit solvation model would compete with explicit solvents in solvating the charged species, creating a “cavity shell” that cannot properly describe hydration behaviors. As a result, the ΔG of the Volmer step from FPMD-TI method would be unreliable, due to the generation of the hydroxide anion in the final state. The IS-TS section of the free energy profile involves no charged species and can yield reliable barrier. Therefore, we only discuss the barriers and the structural evolutions in the IS-TS section of the reaction profiles.

Data availability

All data are available in the manuscript or the Supplementary Information. Source data are provided with this paper. The scripts for performing fixed-potential molecular dynamics simulations are open-sourced at the public repository https://github.com/zishengz/echo and can be accessed free of charge.

Notes

The authors declare no competing financial interests.

Acknowledgments. X.D. acknowledges support from the National Science Foundation award 1800580. Y.H. acknowledges support from the Office of Naval Research by grant number N000141812155. A.N.A. acknowledges support by DOE-BES grant DE-SC0019152. Q.J. acknowledges the beamlines 7-BM (QAS) and 8-ID (ISS) of the National Synchrotron Light Source II, a DOE Office of Science User Facility operated for the DOE Office of Science by Brookhaven National Laboratory under contract no. DE-SC0012704 for XAS measurements. A.N.A. acknowledges the computational and storage resources from the National Energy Research Scientific Computing Center (NERSC), a U.S. Department of Energy Office of Science User Facility operated under Contract No. DE-AC02-05CH11231. HAADF imaging and EDS mapping were carried out using the JEOL Grand ARM in the Irvine Materials Research Institute at the University of California, Irvine.

Author contributions. X.D., Y.H. and C.W. designed the research. C.W. performed the synthesis, most of the structural characterizations, electrochemical tests and analysis. Q.S., E.L., and Q.J, carried out the XAS measurements and Q.J. analyzed the spectra. Z.Z. and A.N.A. conducted DFT calculations. S.W., H.P., Z.C., A.H.S., and X.F. assisted in the synthesis, preparation of XAS electrode and electrochemical tests. H.P. and A.Z. conducted the aberration-corrected STEM characterization. The paper was co-written by C.W., Z.Z., A.N.A. Y.H. and X.D. The research was supervised by X.D., Y.H., and A.N.A. All authors discussed the results and commented on the manuscript.

References

1 Liu, M., Zhao, Z., Duan, X. & Huang, Y. Nanoscale structure design for high-performance Pt-Based ORR catalysts. *Adv. Mater.* **31**, 1802234 (2019).

2 Huang, J. et al. Experimental Sabatier plot for predictive design of active and stable Pt-alloy oxygen reduction reaction catalysts. *Nat. Catal.* **5**, 513-523 (2022).

3 Wan, C., Duan, X. & Huang, Y. Molecular design of single-atom catalysts for oxygen reduction reaction. *Adv. Energy Mater.* **10**, 1903815 (2020).

4 Liu, K. et al. Insights into the activity of single-atom Fe-N-C catalysts for oxygen reduction reaction. *Nat. Commun.* **13**, 2075 (2022).

5 Wang, J. et al. Design of N-coordinated dual-metal sites: A stable and active Pt-free catalyst for acidic oxygen reduction reaction. *J. Am. Chem. Soc.* **139**, 17281-17284 (2017).

6 Wang, X. et al. Review of metal Catalysts for oxygen reduction reaction: from nanoscale engineering to atomic design. *Chem* **5**, 1486-1511 (2019).

7 Sheng, W. et al. Correlating hydrogen oxidation and evolution activity on platinum at different pH with measured hydrogen binding energy. *Nat. Commun.* **6**, 5848 (2015).

8 Zheng, J., Sheng, W., Zhuang, Z., Xu, B. & Yan, Y. Universal dependence of hydrogen oxidation and evolution reaction activity of platinum-group metals on pH and hydrogen binding energy. *Science Advances* **2**, e1501602 (2016).

9 Sheng, W., Myint, M., Chen, J. G. & Yan, Y. Correlating the hydrogen evolution reaction activity in alkaline electrolytes with the hydrogen binding energy on monometallic surfaces. *Energy Environ. Sci.* **6**, 1509-1512 (2013).

10 Zheng, J., Nash, J., Xu, B. & Yan, Y. Perspective—towards establishing apparent hydrogen binding energy as the descriptor for hydrogen oxidation/evolution reactions. *J. Electrochem. Soc.* **165**, H27-H29 (2018).

11 Cheng, T., Wang, L., Merinov, B. V. & Goddard, W. A. Explanation of dramatic pH-dependence of hydrogen binding on noble metal electrode: greatly weakened water adsorption at high pH. *J. Am. Chem. Soc.* **140**, 7787-7790 (2018).

12 Briega-Martos, V., Ferre-Vilaplana, A., Herrero, E. & Feliu, J. M. Why the activity of the hydrogen oxidation reaction on platinum decreases as pH increases. *Electrochim. Acta* **354**, 136620 (2020).

13 Li, P. et al. Hydrogen bond network connectivity in the electric double layer dominates the kinetic pH effect in hydrogen electrocatalysis on Pt. *Nat. Catal.* **5**, 900-911 (2022).

14 Li, J. et al. Experimental proof of the bifunctional mechanism for the hydrogen oxidation in alkaline media. *Angew. Chem. Int. Ed.* **56**, 15594-15598 (2017).

15 Subbaraman, R. et al. Trends in activity for the water electrolyser reactions on 3d M(Ni,Co,Fe,Mn) hydr(oxy)oxide catalysts. *Nat. Mater.* **11**, 550-557 (2012).

16Strmcnik, D. et al. Improving the hydrogen oxidation reaction rate by promotion of hydroxyl adsorption. *Nat. Chem.* **5**, 300-306 (2013).

17 Subbaraman, R. et al. Enhancing hydrogen evolution activity in water splitting by tailoring Li^+-$Ni(OH)^2$-Pt interfaces. *Science* **334**, 1256-1260 (2011).

18 Rebollar, L. et al. “Beyond adsorption” descriptors in hydrogen electrocatalysis. *ACS Catal.* **10**, 14747-14762 (2020).

19 Wang, Y.-H. et al. Spectroscopic verification of adsorbed hydroxy intermediates in the bifunctional mechanism of the hydrogen oxidation reaction. *Angew. Chem. Int. Ed.* **60**, 5708-5711 (2021).

20 Lin, X.-M. et al. In situ probe of the hydrogen oxidation reaction intermediates on PtRu a bimetallic catalyst surface by core–shell nanoparticle-enhanced Raman spectroscopy. *Nano Lett.* **22**, 5544-5552 (2022).

21 Liu, E. et al. Interfacial water shuffling the intermediates of hydrogen oxidation and evolution reactions in aqueous media. *Energy Environ. Sci.* **13**, 3064-3074 (2020).

22 Rizo, R. et al. Investigating the presence of adsorbed species on Pt steps at low potentials. *Nat.* Commun. **13**, 2550 (2022).

23 Shah, A. H. et al. The role of alkali metal cations and platinum-surface hydroxyl in the alkaline hydrogen evolution reaction. *Nat. Catal.* **5**, 923-933 (2022).

24 Liu, E., Jiao, L., Jia, Q. & Mukerjee, S. Through the interface: New insights of the hydrogen evolution and oxidation reactions in aqueous solutions. *Electrochem. Sci. Adv.* **00**, e202300016 (2023).

25 Zhu, S. et al. The role of ruthenium in improving the kinetics of hydrogen oxidation and evolution reactions of platinum. *Nat. Catal.* **4**, 711-718 (2021).

26 McCrum, I. T. & Koper, M. T. M. The role of adsorbed hydroxide in hydrogen evolution reaction kinetics on modified platinum. *Nat. Energy* **5**, 891-899 (2020).

27 Li, M. et al. Platinum–water interaction induced interfacial water orientation that governs the pH-dependent hydrogen oxidation reaction. *J. Phys. Chem. Lett.* **13**, 10550-10557 (2022).

28 Huang, B. et al. Cation- and pH-dependent hydrogen evolution and oxidation reaction kinetics. *JACS Au* **1**, 1674-1687 (2021).

29 Darlington, A. M. et al. Separating the pH-dependent behavior of water in the stern and diffuse layers with varying salt concentration. *J. Phys. Chem. C* **121**, 20229-20241 (2017).

30 Ledezma-Yanez, I. et al. Interfacial water reorganization as a pH-dependent descriptor of the hydrogen evolution rate on platinum electrodes. *Nat. Energy* **2**, 17031 (2017).

31 Zhan, C. et al. Subnanometer high-entropy alloy nanowires enable remarkable hydrogen oxidation catalysis. *Nat. Commun.* **12**, 6261 (2021).

32 Scofield, M. E. et al. Role of chemical composition in the enhanced catalytic activity of Pt-Based alloyed ultrathin nanowires for the hydrogen oxidation reaction under alkaline conditions. *ACS Catal.* **6**, 3895-3908 (2016).

33 Wang, M. et al. Ultrafine platinum-iridium distorted nanowires as robust catalysts toward bifunctional hydrogen catalysis. *J. Mater. Chem. A* **10**, 18972-18977 (2022).

34 Panigrahy, S., Samanta, R., Panda, P., Mishra, R. & Barman, S. RuO2 as promoter in Pt-RuO2-nanostructures/carbon composite, a pH-universal catalyst for hydrogen evolution/oxidation reactions. *Int. J. Energy Res.* **46**, 6406-6420 (2022).

35 Jin, Y. et al. Lamellar platinum–rhodium aerogels with superior electrocatalytic performance for both hydrogen oxidation and evolution reaction in alkaline environment. *J. Power Sources* **435**, 226798 (2019).

36 Yang, Y. et al. Electronic modulation of Pt nanoparticles on Ni3N–Mo2C by support-induced strategy for accelerating hydrogen oxidation and evolution. *J. Phys. Chem. Lett.* **13**, 2107-2116 (2022).

37 Qin, B. et al. A novel IrNi@PdIr/C core–shell electrocatalyst with enhanced activity and durability for the hydrogen oxidation reaction in alkaline anion exchange membrane fuel cells. *Nanoscale* **10**, 4872-4881 (2018).

38 Mao, J. et al. Isolated Ni atoms dispersed on Ru nanosheets: High-performance electrocatalysts toward hydrogen oxidation reaction. *Nano Lett.* **20**, 3442-3448 (2020).

39 Liu, D. et al. One-pot synthesis of IrNi@Ir core-shell nanoparticles as highly active hydrogen oxidation reaction electrocatalyst in alkaline electrolyte. *Nano Energy* **59**, 26-32 (2019).

40 Qiu, Y. et al. BCC-phased PdCu alloy as a Highly active electrocatalyst for hydrogen oxidation in alkaline electrolytes. *J. Am. Chem. Soc.* **140**, 16580-16588 (2018).

41 Bard, A. J., Faulkner, L. R. & White, H. S. *Electrochemical methods: Fundamentals and applications*. (John Wiley & Sons, 2022).

42 Greeley, J. & Mavrikakis, M. Surface and subsurface hydrogen: adsorption properties on transition metals and near-surface alloys. *J. Phys. Chem. B* **109**, 3460-3471 (2005).

43 Kunimatsu, K., Uchida, H., Osawa, M. & Watanabe, M. In situ infrared spectroscopic and electrochemical study of hydrogen electro-oxidation on Pt electrode in sulfuric acid. *J. Electroanal. Chem.* **587**, 299-307 (2006).

44 Lindgren, P., Kastlunger, G. & Peterson, A. A. A challenge to the G ∼ 0 interpretation of hydrogen evolution. *ACS Catal.* **10**, 121-128 (2020).

45 Garcia-Araez, N., Climent, V. & Feliu, J. Potential-dependent water orientation on Pt(111), Pt(100), and Pt(110), as inferred from laser-pulsed experiments. electrostatic and chemical effects. *J. Phys. Chem. C* **113**, 9290-9304 (2009).

46 Xing, Y.-F. et al. Bifunctional mechanism of hydrogen oxidation reaction on atomic level tailored-Ru@Pt core-shell nanoparticles with tunable Pt layers. *J. Electroanal. Chem.* **872**, 114348 (2020).

47 Arruda, T. M. et al. Fundamental aspects of spontaneous cathodic deposition of Ru onto Pt/C electrocatalysts and membranes under direct methanol fuel cell operating conditions: an in Situ X-ray absorption spectroscopy and electron spin resonance study. *J. Phys. Chem. C* **114**, 1028-1040 (2009).

48 Jia, Q. et al. Activity descriptor identification for oxygen reduction on platinum-based bimetallic nanoparticles: in Situ observation of the linear composition–strain–activity relationship. *ACS Nano* **9**, 387-400 (2015).

49Newville, M. IFEFFIT : Interactive XAFS analysis and FEFF fitting. *J. Synchrotron Radiat.* **8**, 322-324 (2001).

50 Ravel, B. & Gallagher, K. Atomic structure and the magnetic properties of Zr-Doped Sm2Co17. *Phys. Scr.* **2005**, 606 (2005).

51 Newville, M., Limacrvincedilscaron, P., Yacoby, Y., Rehr, J. J. & Stern, E. A. Near-edge x-ray-absorption fine structure of Pb: A comparison of theory and experiment. *Phys. Rev. B* **47**, 14126 (1993).

52 Ankudinov, A. L., Ravel, B., Rehr, J. J. & Conradson, S. D. Real-space multiple-scattering calculation and interpretation of x-ray-absorption near-edge structure. *Phys. Rev. B* **58**, 7565-7576 (1998).

53 Jorgensen, W. L., Chandrasekhar, J., Madura, J. D., Impey, R. W. & Klein, M. L. Comparison of simple potential functions for simulating liquid water. *J. Chem. Phys.* **79**, 926-935 (1983).

54 Adamo, C. & Barone, V. Toward reliable density functional methods without adjustable parameters: The PBE0 model. *J. Chem. Phys.* **110**, 6158-6170 (1999).

55 Kresse, G. & Joubert, D. From ultrasoft pseudopotentials to the projector augmented-wave method. *Phys. Rev. B* **59**, 1758-1775 (1999).

56 Kresse, G. & Furthmüller, J. Efficiency of ab-initio total energy calculations for metals and semiconductors using a plane-wave basis set. *Comput. Mater. Sci.* **6**, 15-50 (1996).

57 Kresse, G. & Furthmüller, J. Efficient iterative schemes for ab initio total-energy calculations using a plane-wave basis set. *Phys. Rev. B* **54**, 11169-11186 (1996).

58 Kresse, G. & Hafner, J. Ab initio molecular dynamics for liquid metals. *Phys. Rev. B* **47**, 558-561 (1993).

59 Kresse, G. & Hafner, J. Ab initio molecular-dynamics simulation of the liquid-metal--amorphous-semiconductor transition in germanium. *Phys. Rev. B* **49**, 14251-14269 (1994).

60 Grimme, S., Antony, J., Ehrlich, S. & Krieg, H. A consistent and accurate ab initio parametrization of density functional dispersion correction (DFT-D) for the 94 elements H-Pu. *J. Chem. Phys.* **132** (2010).

61 Mathew, K., Kolluru, V. S. C., Mula, S., Steinmann, S. N. & Hennig, R. G. Implicit self-consistent electrolyte model in plane-wave density-functional theory. *J. Chem. Phys.* **151** (2019).

62 Yu, M. & Trinkle, D. R. Accurate and efficient algorithm for Bader charge integration. *J. Chem. Phys.* **134** (2011).

63 Steinmann, S. N., Michel, C., Schwiedernoch, R. & Sautet, P. Impacts of electrode potentials and solvents on the electroreduction of CO_2: a comparison of theoretical approaches. *Phys. Chem. Chem. Phys.* **17**, 13949-13963 (2015).

64 Duan, Z. & Henkelman, G. Atomic-scale mechanisms of electrochemical Pt dissolution. *ACS Catal.* **11**, 14439-14447 (2021).

65 Korpelin, V. et al. Addressing dynamics at catalytic heterogeneous interfaces with DFT-MD: Anomalous temperature distributions from commonly used thermostats. *J. Phys. Chem. Lett.* **13**, 2644-2652 (2022).

66 Zhao, X. & Liu, Y. Origin of selective production of hydrogen peroxide by electrochemical oxygen reduction. *J. Am. Chem. Soc.* **143**, 9423-9428 (2021).